

Determination of Flutter Angle by Resolving Effective Gyroscope Couple to Retard Air Resistance in Aeroplane

Srivardhan.R¹, Vishal.S², Balasubramanyam D.B³, Dharshanaa G.B⁴

¹Student, Dept. of Mechanical Engineering, Chennai Institute of technology, Chennai, India.

²Student, Dept. of Mechanical Engineering, Chennai Institute of technology, Chennai, India.

³Student, Dept. of Computer Science and Engineering, Chennai Institute of technology, Chennai, India.

⁴Student, Dept. of Computer Science and Engineering, Chennai Institute of technology, Chennai, India.

Abstract

The paper discusses how to effectively resolve a gyroscope couple for a three-dimensional working model in order to achieve the deflection in all three coordinates in a simple and straightforward manner. Furthermore, the flutter is programmed to perform tilt of it in order to include proper uplift and displacement is tested with the aid of a finite element model in an efficient manner and adaptive to incorporate and identified and resolved.

Key Words: Flutter, deflection, resistance, effective couple, magnitude,

1. INTRODUCTION:

The primary objective of this research is to determine the impact of a vast wing-tip fin, which is an oversized version of contemporary winglets, on flutter speed. The dissemination of information concerning static aeroelastic behaviour, which could also alter the excellent traction of vertical surfaces mounted only at tip, is a major priority. To accomplish this, then a concise overview of winglet flutter is examined. The results for a general configuration using a straightforward model and a higher-fidelity flutter model are then presented. Winglets are used by a number of modern commercial aircraft to mitigate induced drag at yacht charter speeds. Flutter is not a concern with these aircraft since they have been certified following a thorough analysis, test, and certification process Presented as 53rd AIAA Structures. However, since the gyroscope is a critical component of the navigation system and is frequently used to achieve the measurement of the system's attitude, there is very little archival research on the impact of winglets on flutter.

Gyroscope stability has a big impact on the transponder, and it plays a big part in stability control, navigation, and assistance. Correspondingly, it is vital. The navigation system is severely influenced by its stability. Consequently, it's pivotal to research gyroscope fault diagnosis advanced technologies. Due to the gyroscope malfunction, the redundancy of the remaining operating gyroscope cannot appease the parity equation for fault

diagnosis during the chronic conditions of the navigation system. As either a consequence, other methods must be employed to diagnose gyroscope faults. It is challenging to create concise computational equations for the measurement and control components of dynamical system, and the existing analytical redundancy method struggles to satisfy the requirements of fault diagnosis. . The researchers suggested a fault diagnosis and diagnosis based on signal processing and knowledge-based methods to address the aforementioned limitations. Information fusion and wavelet analysis are two common techniques based on signal processing.

2. MATERIALS AND METHODS:

The benefit of a gyroscope condition monitoring technology based on wavelet transform is that it can undertake time-frequency comprehensive analysis on sensor signals, which can rapidly and aptly diagnose faults.[3] The quantification information for multi-sensor systems is complex and diverse, so the information fusion method must also be reliable, fault-tolerant, and resilient. A noteworthy outcome was attained.

2.1 Configuration of redundancy in gyroscope

Two or more identical gyroscopes can be utilized for redundant configuration design in the stance measurement system to complete the system attitude measurement 20-21. This study employs three redundant three-degree-of-freedom gyroscopes, each of which is capable of measuring the angular velocity of three orthogonal axes. When a gyroscope's measured value for one of its axes is

$$m = w \cos \alpha + \varepsilon \quad (1)$$

Specify the standard deviation as follows:

$$\varepsilon_N = \frac{\varepsilon}{w_i \cos \alpha}$$

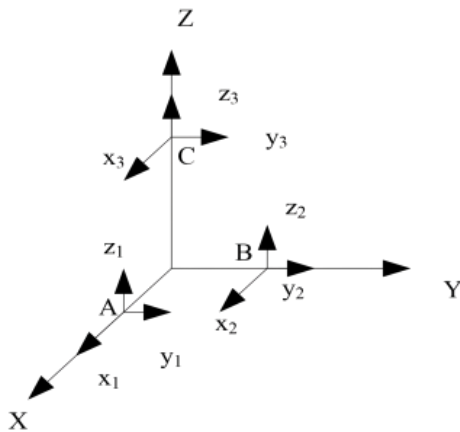


Fig. 1 gyroscope redundancy configuration scheme

The data packets of the three axis of the gyroscopes are A, B, and C, respectively. The multiple evaluation axes of the gyroscope A are x_1, y_1, z_1 ; the three measuring axes of the gyroscope B are X_2, Y_2, Z_2 ; the three measuring axes of the gyroscope C are X_3, Y_3, Z_3 . The arrangement of a three-axis gyroscopes and the arrangement orientations of the x, y and z axes of every three-axis gyroscope are depicted in Fig. 1. There are nine hypersensitive axes in the setup method, and the robust strong support system parameters of the three-axis gyroscope.

2.2 Stability in upright condition

The simplest way to utilize a gyroscope to stabilize flight motions is to take advantage of the natural dynamics of the vehicle. In previous work [1] it was shown analytically and $mg \theta \times f_d \times X \times Z \times Y$ table (1): Model and axis convention for the robotic fly. The vehicle state is given by three quantities, the rotation angle θ , the rotation velocity ω , and the lateral velocity in body coordinates v . A lift force f_l generated by the flapping wings acts at a distance right away from the center of mass and along the body-z direction, an aerodynamic drag force forward acts at a distance rightward from the CM,[4] and the gravitational force mg acts at the center of mass. The right-handed axis convention for world coordinates is shown, with y pointing into the paper. A feedback controller applies a control torque (τ) by altering baseline wing kinematics.

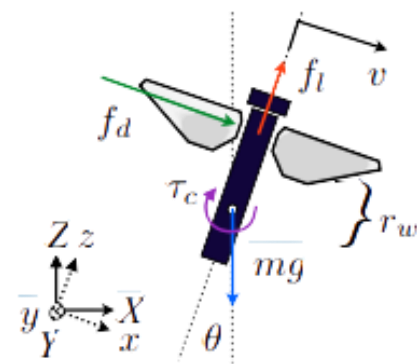


Fig. 2 couple forces acting on the gyroscope configuration

2.3 development of model:

Designers picked this aircraft due of its vast documentation. Two analytical models were created. The first and simplest model is a Rayleigh-Ritz beam model, in which the wing and fin components are both modelled as homogeneous beams with bending and torsional degrees of freedom. A quasi-steady aerodynamic approximation for the unsteady forces and moments offers an airspeed dependent aerodynamic stiffness. This type restricts the tip-fin to be installed in a vertical position only. Wing deformation involves two presumed displacement modes, one for bending and the other for torsion. The displacement at any point on the wing surface, $w(x, y, t)$, is comprised of upward bending at the wing shear centre, w_{SC} , and twist about the shear centre, θ [2],[1]. In terms of the wing spanwise coordinate, y , measured outward from the cantilevered wing root, and the chordwise coordinate, x , measured aft from the wing elastic axis, the displacement of any point on the wing is

Parameters			
Basic parameters	Time	Steady	
	Type	based on Pressure-	
Models	Viscous model	k-omega (2-eqn) SST	
Materials	Fluid	Air	
	Density	Incompressible-ideal-gas	
	Viscosity	Constant	1.7894e-05
Boundary conditions	Inlet	Velocity	0-90 [km/h]
		Turbulent intensity [%]	1
		Turbulent length scale [m]	0.28

Outlet	Pressure-outlet	gauge pressure 0 Pa
	Turbulent intensity [%]	1
	Turbulent length scale rml	0.28

Table 1. Parameters of gyroscopic couple

$$w_1 = W_{wing}(x, y_w, t) = w_{sc}(y_w, t) - x\beta(y_w, t) \quad (2)$$

The tip-fin motion is made of two separate forms of motion. The first is designated as w_2 and is due to out-of-plane fin bending and torsion, a function of the fin spanwise coordinate, y_f , and the fin chordwise coordinate, x_f .

$$w_2 = w_f(x_f, y_f, t) = W_{fin,SC} - X_f\beta_f \quad (3)$$

The wing mass is given by a sequence of concentrated mass components whose distance from the spar may be modified to regulate the chordwise centre of gravity (c.g.) location. The tip-fin mass and stiffness characteristics are similar as the wing; tip-fin length and cant angle are parameters for this model [5]. The geometry and material properties for the finite element model were identical to the Rayleigh-Ritz, wing model, but a doublet lattice, precarious aerodynamic forces framework replaced the streamlined quasistatic aerodynamic representation, whereas the assumed structural deflection modes were replaced by a finite element structural model.

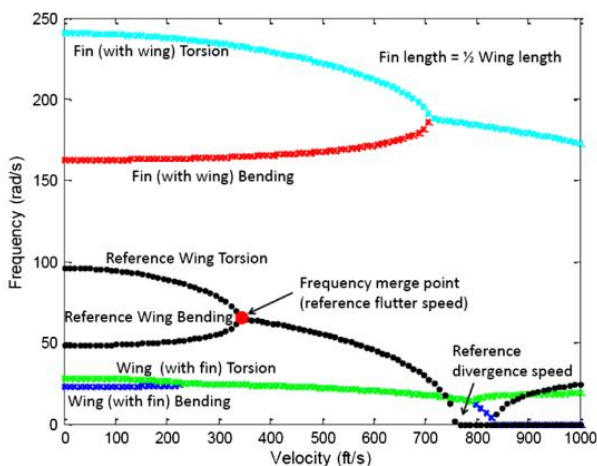


Fig.3 Comparison of frequency merging, wing without tip-fin, wing with tip-fin.

$$[w^2 ml^3 [M_i]] \{a_i\} + \{[K_{i,j}]\} \{a_i\} - [Q_i] \{q_i\} = \{0\} \quad (3)$$

$$-[M_i] + [K_i] \{a\} = \{0\} \quad (4)$$

$$\Omega^2 = \frac{ml^4}{EI} \omega^2 \quad (5)$$

The mass, stiffness, and aerodynamic force matrices are calculated using expressions for the wing/tip-fin kinetic energy, the wing/tip-fin strain energy, and the virtual work done by the quasi-steady aerodynamic forces acting on the wing and tip-fin. The result, using Lagrange's equations and assuming harmonic motion, is a fourth order eigenvalue.

2.4 Feedback from motion capture

Figure 3 illustrates that, with suitable tuning of controller gains and trim settings, the robot was able to bear the extra weight and lift off and hover around the intended setpoint location $[X, Y, Z] T = [0.04362, 0.04988, 0.05866] T m$ utilizing motion capture feedback. Its mean location for the 2 s time after attaining the required height was $[0.053, 0.005, 0.062] T m$.

2.5 Feedback from angular velocity

After verifying the angular velocity estimate of ω from the gyroscope accurately matches the ground truth measurement from motion capture, with lower 0.08 0.1 0.12 0.14 0.16 -0.02 0 0.02 0.04 0.06 0 0.02 0.04 0.06 0.08 y (m) x (m) z (m) (m) Figure 3: Plot of hovering flight trajectory in which gyroscope supplied an estimate of the angular velocity ω . Other characteristics are the same as in Figure (4), [7]. delay, we included this estimate into the hovering attitude controller. Figure 8 demonstrates that the robot accomplishes hovering flight, flying near the specified point, maintaining a mean position of $[0.04362, 0.04988, 0.05866] N- m$ and equivalent error.

2.6 Control algorithm

This code accepts the resolver components x, y, and z from the gyroscope as inputs and passes them to the function. For the purpose of predicting flatter angles, the function makes use of conditional statements. Conditional statements change the behaviour of the code based on a set of inputs. The angle of deflection in a coordinate is returned by this function. A set of values determines specific commensuration. A deflection of 13 degrees in the x-axis is observed when the x component is subject to a force of 0.04362, and y and z experience forces less than 0.005 and 0.062 respectively. Force of 0.04988 in the y component causes the y coordinate to deviate by 8 degrees while the force is less than 0.053 and 0.062 in x and z. A force of 0.05866 in the z component causes a 12-degree deflection where x and y remain less than 0.053 and 0.005 respectively. While the

y component experiences the same amount of force but x and z do not match 0.053 and 0.062, a 5-degree deviation is observed. The inputs are considered to be invalid if they do not pass any of the above conditions.

```
def flatterAngle(inp):
    x,y,z = inp[0],inp[1],inp[2]
    if x == 0.04362 and y < 0.005 and z <=0.062 :
        return 13 #deflection in x-axis
    elif x <= 0.053 and y == 0.04988 and z <= 0.062 :
        return 8 #deflection in y-axis
    elif x <= 0.053 and y < 0.005 and z == 0.05866 :
        return 12 #deflection in z-axis
    elif x != 0.053 and y < 0.005 and z != 0.062 :
        return 5 #deflection for special case
    else:
        return 'Invalid Input'
    n = int(input())
    for i in range(n):
        inp = list(map(float,input().split()))
        print(flatterAngle(inp))
```

3. ANALYSIS

The flight utilising solely motion capture estimations yielded a mean Euclidean distance error of less than 0.01 m from the setpoint. When the ω estimate from the gyroscope was added, the mean inaccuracy was a similar 0.01 m. For the flight in which gyroscope feedback additionally calculated the attitude \hat{z} , the inaccuracy rose to 0.03 m. A probable reason for the mistake is that, as can be shown in Figure 4, a clear drift is observable along the pitch (red) axis, reaching an error of 6° (0.1 rad) (0.1 rad). This drift, probably emerging because the biggest oscillations occur along this axis due of the forward-backward movements of the wings (Figure 3), would generate a force inaccuracy in the y-direction when the vehicle tilted in response. In addition to showing the 3D trajectory of each flight and comparing the mean location of each flight experiment, we determined the root mean square error (RMSE- Root Mean Square Error) see Figure 4). We predict comparable amounts of RMSE in altitude because coordinates, 0.05 0.068 0.12, 0.02 0.04 0.06, y (m) x (m)

z (m) (m) Figure 5: Plot of flight trajectory in which the gyroscope gave entire attitude feedback in the flight controller, including both angular velocity ω and attitude \hat{z} . In this flight, the position error was somewhat greater than in Figure (6), presumably due of drift in the attitude estimate. Other characteristics are the same as in Figure (7). the altitude controller operates independently of the attitude controller and gets the identical values in all testing, as can be noted in Figure 8. RMSE is comparable between the motion capture-only experiment and experiment in which the gyroscope calculated ω for both x-position, where the errors are 1.17 cm and 1.39 cm, respectively, as well as for the y-position, where the errors are 1.26 cm and 1.05 cm, respectively. The RMSE of the lateral position of the aircraft using attitude estimate from the gyroscope is much bigger at 2.72 cm in x-position and 2.95 cm in y-position. [7] Given that the robot had trouble regulating its pitch angle and wandered away from the set position during flight, these figures are not surprising. These results demonstrate that estimations from the gyroscope may be replaced for those from the motion capture system and still retain stability and control of the vehicle despite its quick and unstable dynamics.

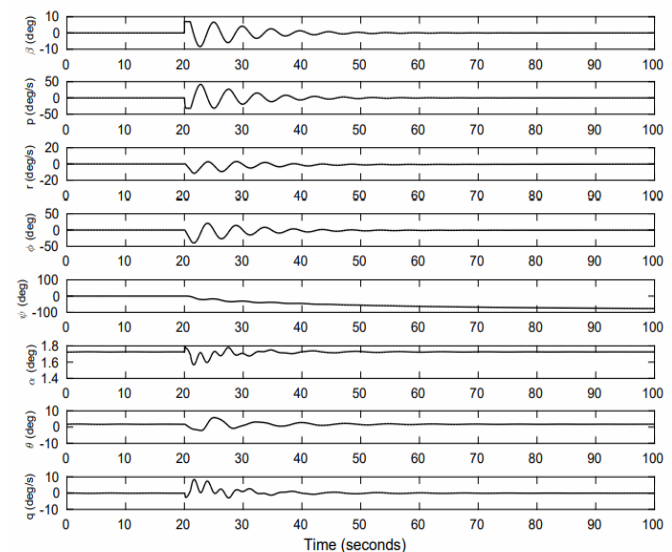


Fig.4 Response of gyroscope at x axis.

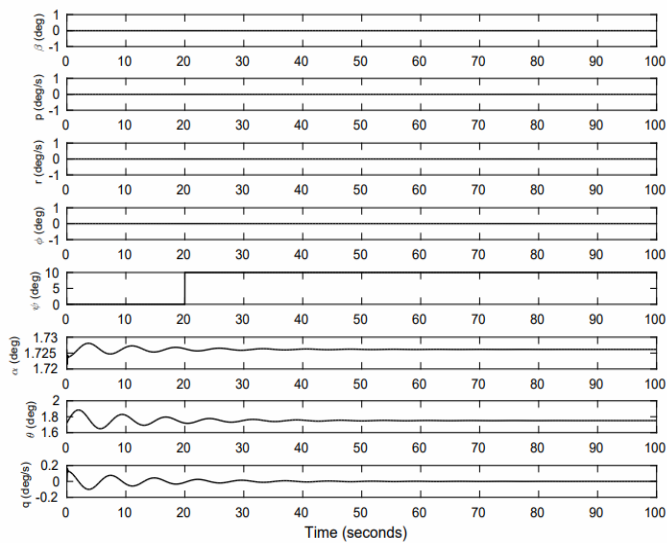


Fig.5 Response of gyroscope at y axis:

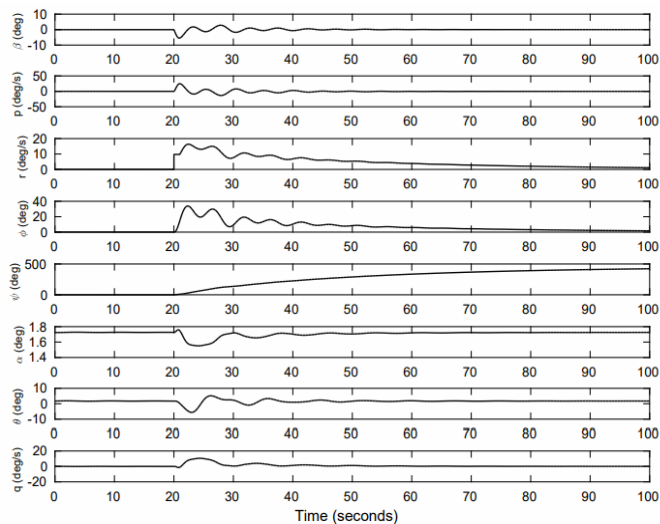


Fig.6 Response of gyroscope at z axis:

4. FLUTTER RESULTS:

Figure 5 displays typical flutter results from the Rayleigh-Ritz quasi-steady model with a 90 degrees can't angle tip-fin length (L_f), half the wing semi-span(L). The set of black lines plot the real sections of the system eigenvalues for the wing without a fin. Flutter is represented by the coalescence of the wing-bending and torsion modes. When the fin is added to the wing, four eigenvalues occur and there are two separate frequency coalescence curves. One of these curves will merge at a lower flutter speed, depending on the fin size compared to the wing. The lower set of curves, blue and green, demonstrate flutter initiation caused predominantly by wing bending torsion interaction. This motion is adjusted by the tip-fin. The second set of curves, the top set of blue and red lines, merge at a greater velocity; this

interaction is principally between the tip-fin bending and torsion motion modified by wing-tip motion at the tip-fin base connection. The relative placements of these two coalescence sites alter with fin length. In this scenario, the flutter speed is lowered by the insertion of the tip-fin. Figure 7 illustrates flutter data from the two models illustrating how flutter speed varies as tip-fin length grows when the tip-fin is vertical. The findings displayed in Fig. 8 are also standardised to the speeds predicted by each model for the wing without the tip-fin. The ASTROS model always forecasts higher flutter speeds than the quasistatic model. The ASTROS model suggests that flutter speed is reduced when even a little fin is added to the wing, however the quasi-steady model shows a modest increase in flutter speed for small fins. Both models reveal that as the fin length grows, the flutter speed is lowered to less than half of the no-fin value. These results are similar with the previously reported research in [5], [9], and [10] when the fin is very tiny. Both models imply that there are two flutter modes and indicate that there is a flutter mode switching occurrence near $L_f/L \approx 0.5$ when the tip-fin gets large enough to trigger the flutter instability.

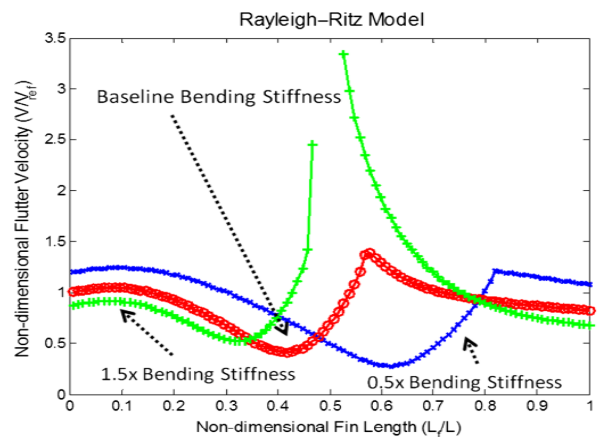


Fig.7 Results of Rayleigh's model based on flutter.

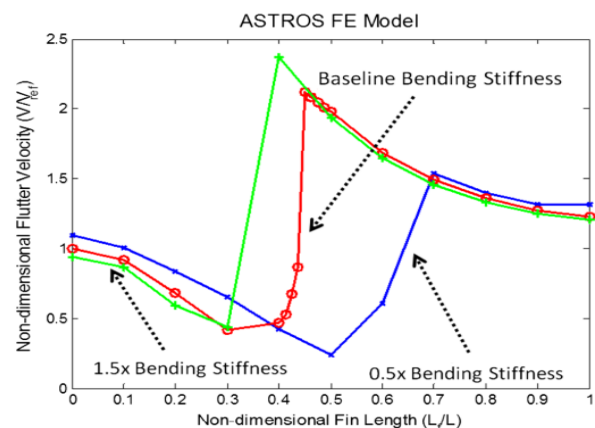


Fig.8 . Results of Astros' model based on flutter.

4.1 Static aeroelasticity-directional stability derivatives

The value of the lift-curve slope of a stiff swept surface drops approximately in relation to $\cos(\Lambda)$. This compensates for this drop in side-force caused by sideslip.[10] The flexible fin side-force stability derivative drops as well, but the figure also indicates that at moderate sweep angles the adjustable fin is more effective, but as the fin is swept the pliable surface is far less effective. At increasing sweep angles, fin yielding coupled with fin sweep diminishes the efficiency of the fin.[6] The yaw-moment flexible derivative demonstrates similar behaviour to the flexible side-force derivative. However, observe that the stiff stability component initially decreases (greater stability) but the curve has a local minimum at approximately 20 deg. As the fin is swept, the fin lift-curve slope reduces as the moment arm between the fin aerodynamic centre and the fuselage centre of gravity grows. Initially, the moment arm increase is higher than the lift-curve slope drop, and therefore the fin offers more yaw stability. However, with bigger fin sweep angles, as sweep angle increases, fin bending coupling with fin sweep diminishes the efficiency of the fin. The hard surface yaw components for the larger, longer fin alter in a similar method to the smaller fin rigid yaw derivatives. However, the crossover (the point when the flexible surface becoming less efficient than the rigid surface) takes place at a lower sweep angle. Also, for high sweep angles, 35 to 45 degrees, the shorter fin's flexible side force component magnitude is bigger (more adverse) than the larger fin's. Based on the sweep angle the fin, this could be concern for vehicles dependent on tip-fins for directional stability.

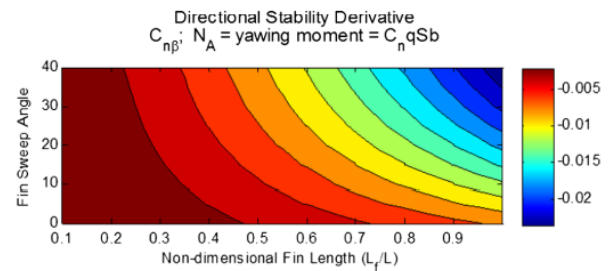
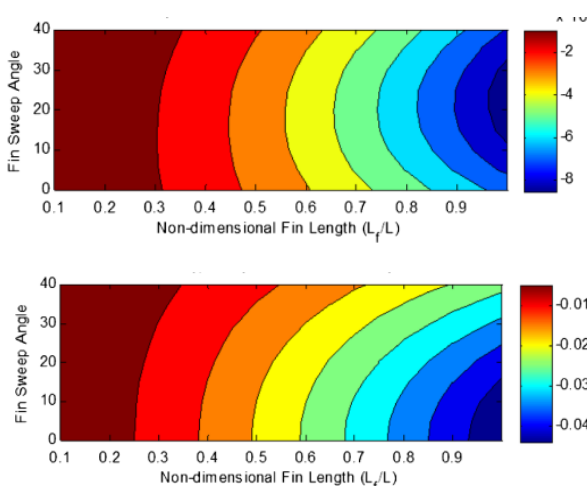


Fig.9 . Results finite element model based on flutter

5.0 CONCLUSION:

Placing fins on wing tips as a substitute for a vertical tail presents two aeroelastic challenges, one dynamic, the other will be static.[8] The results reported in this paper demonstrate that the tip-fin size, notably the tip-fin length, and its cant angle are essential design features that affect flutter speed. The user is reminded that the boundary conditions adopted for these experiments preclude the influence of body freedom or anti-symmetric modes of flutter. Small fins aim to limit flutter speed whereas mode switching may allow very lengthy fins to improve flutter speed. Static aeroelastic effects also influence vehicle directional/yaw stability, largely via variations in lifting surface efficacy, a well-known phenomenon for swept and upswept flight controls. These effects are likewise governed by tip-fin levels equivalent to the wing size and also by wing sweep.

6.0 REFERENCE:

[1] Kiyari, R.; Kim, S.K.; Kim, B.Y. Bidirectional single-mode Er-doped fiber-ring laser. *IEEE Photonics Technol. Lett.* 1996, 8, 1624–1626. [CrossRef]

[2] Cai, H.; Zhang, H.; Zheng, Y. Soft Magnetic Devices Applied for Low Zero Excursion Ring Laser Gyro. *IEEE Trans. Magn.* 2007, 43, 2686–2688. [CrossRef]

[3] Mignot, A.; Feugnet, G.; Schwartz, S.; Sagnes, I.; Garnache, A.; Fabre, C.; Pocholle, J.P. Single-frequency external-cavity semiconductor ring-laser gyroscope. *Opt. Lett.* 2009, 34, 97–99. [CrossRef] [PubMed]

[4] Schwartz, S.; Gutty, F.; Feugnet, G.; Loil, É.; Pocholle, J. Solid-state ring laser gyro behaving like its helium-neon counterpart at low rotation rates. *Opt. Lett.* 2009, 34, 3884–3886. [CrossRef] [PubMed]

[5] Hurst, R.B.; Stedman, G.E.; Schreiber, K.U.; Thirkettle, R.J.; Graham, R.D. Experiments with an 834 mring laser interferometer. *J. Appl. Phys.* 2009, 105, 113–115. [CrossRef]

[6].. Elliott-Laboratories . *The Anschutz Gyro-Compass and Gyroscope Engineering*. Wexford College Press; Kiel, Germany: 2003. pp. 7–24. [[Google Scholar](#)]

[7].. Honeywell. [(accessed on 24 June 2017)]; Available online: <https://aerospace.honeywell.com/en/products/navigation-and-sensors/inertial-measurement-units>

[8].. King A.D. Inertial Navigation—Forty Years of Evolution. *GEC Rev.* 1998;**13**:140–149. [[Google Scholar](#)]

[9].. Inertial Labs. [(accessed on 24 June 2017)]; Available online: <https://inertiallabs.com/ahrs.html>

[10]. Ezekiel S, Arditty H.J. *Fiber-Optic Rotation Sensors and Related Technologies, Proceedings of the First International Conference MIT, Cambridge, MA, USA, 9–11 November 1981*. Springer-Verlag; Heidelberg, Germany

[11] *Flutter and Directional Stability of Aircraft with Wing-Tip Fins: Conflicts and Compromises | Journal of Aircraft*. (2013, March 30). *Journal of Aircraft*. Retrieved January 29, 2023,